communications earth & environment

Article

A Nature Portfolio journal

https://doi.org/10.1038/s43247-026-03603-y

Rhodoliths can act as daily resolution paleotemperature archives in the Red Sea

Lena Y. Li[1,2] ✉, Juan P. Bernal-Tamayo[3], Steffen Hetzinger[4], Jochen Halfar[5], Walter A. Rich[6], Michael D. Fox[6], Maggie D. Johnson[6], Hubert Vonhof[2], Ralf Schiebel[2] & Bernd R. Schöne[1]

Long-term, high-frequency temperature records are critical for evaluating the vulnerability of marine ecosystems to ongoing ocean warming. Commonly used paleoceanographic archives, such as corals and bivalves, face regional and ecological constraints. Rhodoliths, free-living coralline red algal nodules, are established and globally accessible alternatives, yet their complex three-dimensional growth structures hinder the construction of continuous age models. Here we present a workflow combining staining-based growth calibration, semi-automated increment detection using micro-computed tomography, and dynamic time warping to assemble a daily chronology spanning 133 days (March–July) from seven fruticose thalli of a single rhodolith from the central Red Sea. The resulting multi-thallus chronology, combined with a multi-element temperature proxy (Magnesium-to-Strontium), yields closer agreement with in-situ logger temperatures ($R^2 = 0.91$, RMSE = 0.63 °C) than individual thalli or single-element proxies, establishing a proof-of-concept framework for daily-resolved paleotemperature reconstructions from tropical rhodoliths.

Foundation species such as scleractinian corals and coralline algae construct the physical framework of tropical coral reef ecosystems. These reef structures support approximately 25% of marine biodiversity and generate tens of billions of dollars in annual economic value[1,2]. However, coral reefs are increasingly threatened by rising ocean temperatures[3], which drive widespread habitat loss and functional decline[4]. Assessing reef vulnerability and informing conservation strategies requires an understanding of baseline historical temperature variability at ecologically relevant spatiotemporal scales. Furthermore, while satellite-derived sea surface temperatures (SSTs) provide valuable monthly to daily records, they do not capture the fine-scale temperature fluctuations experienced within coral reefs[5]. This is a critical limitation, as high-frequency temperature variability is a key predictor of organismal stress tolerances and coral bleaching risk[6].

Past environmental variability in reef environments is often reconstructed using the skeletons of corals[7,8], bivalves[9,10], and foraminifers[11,12]. These biogenic carbonates archive physical, structural, and geochemical information that reflects ambient conditions during growth[13]. However, most of the established archives and proxies have limitations. The biogeographic distributions of many species used as archives for the reconstruction of the environment and climate, such as corals and bivalves, are shaped by their environmental tolerances. As ocean conditions change, these suitable habitats are projected to contract, potentially restricting populations to climate refugia and reducing the spatial coverage of available environmental archives[14,15]. Ontogenetic changes, such as shifts in growth rate or the amount of elements incorporated into their skeletons with age, can further complicate chronological reconstruction and geochemical interpretation[16]. In contrast, coralline algae are globally distributed across photic and mesophotic zones[17–20] with minimal ontogenetic effects[21]. Certain species can live for centuries and form seasonal growth bands, offering the potential for high-resolution, long-term environmental reconstructions[22].

While coralline algae have been gaining traction as environmental and climatic archives since the early 2000s[23–26], most proxy work with coralline algae has focused on polar and temperate oceans[27–29], with relatively few studies addressing their utility in tropical and subtropical systems[30,31]. Though coralline algae are also vulnerable to local and global environmental change[32], they are likely to become even more ecologically important as coral reefs change[33], due to their ability to withstand light variability, suppress competing fleshy macroalgae and build and bind reef-frameworks, potentially buffering some of the loss in key ecosystem functions associated with coral declines[34,35].

However, most encrusting coralline algal species grow laterally rather than vertically, making it difficult to distinguish boundaries between

[1]Institute of Geosciences, Johannes Gutenberg University Mainz, Mainz, Germany. [2]Climate Geochemistry, Max Planck Institute for Chemistry, Mainz, Germany. [3]Applied Mathematics and Computational Science, King Abdullah University of Science and Technology, Thuwal, Kingdom of Saudi Arabia. [4]Institute of Geosciences, Christians-Albrechts-University Kiel, Kiel, Germany. [5]Department of Chemical & Physical Sciences, University of Toronto Mississauga, Mississauga, ON, Canada. [6]Biological and Environmental Sciences and Engineering Division, King Abdullah University of Science and Technology, Thuwal, Kingdom of Saudi Arabia. ✉e-mail: lena.li@mpic.de

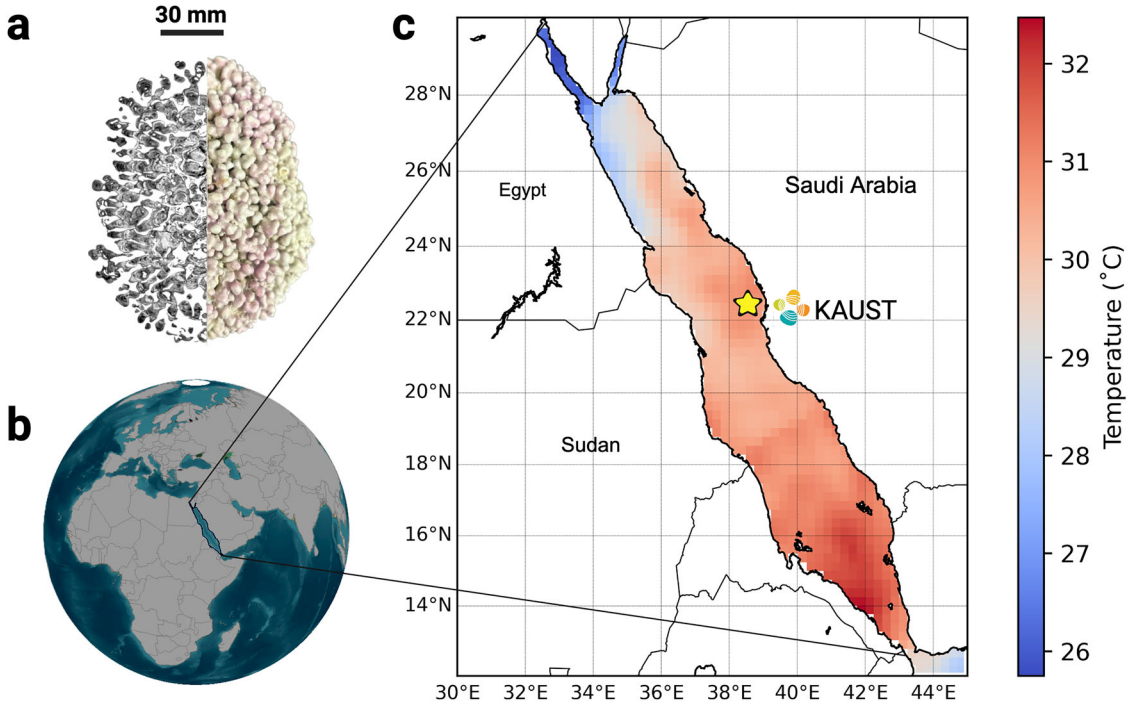

Fig. 1 | Rhodolith sample and study site. a Rhodolith, with the left half showing overview microCT scan (voxel size = 80 µm), and the right half showing the whole, air-dried sample. **b** Map showing location of the Red Sea in a global context (Esri, Maxar, Earthstar Geographics and the GIS User Community). **c** Inset showing the summer sea surface temperature (°C) of the Red Sea (NOAA 1/4° Daily Optimum Interpolation SST). Yellow star indicates sampling locality; logo indicates King Abdullah University of Science and Technology (KAUST).

individuals, which reduces the interpretability of their growth histories. The encrusting forms that do produce the continuous, layered growth that tends to yield higher proxy correlations[36] are largely limited to high-latitude regions[37]. Free-living coralline algae can grow as discrete nodules, termed rhodoliths (or maerl), and are globally distributed across wide depth, temperature, and salinity gradients[32]. Despite this, rhodoliths have been relatively overlooked and underutilized as high-resolution archives because of their complex three-dimensional morphology, variable banding periodicity, and fragmented growth histories[38].

The Red Sea is a valuable system for studying thermal resilience in coral reefs[39]. This semi-enclosed basin is oligotrophic and hypersaline, with high evaporation and intense solar irradiation[40]. Shallow reef flats in the Red Sea experience seasonal temperature ranges of 18 to ~38 °C, and rare events have produced fluctuations greater than 10 °C in a single day[41]. Central and southern Red Sea reef flats frequently reach summer temperatures that match or exceed those projected for many tropical reefs under future high-emissions scenarios[42]. Despite these extremes, the Red Sea hosts the world's second-longest coral reef system, spanning over 2000 km and supporting high endemism.

To address these obstacles, this study sets three objectives: (1) develop a reproducible microcomputed tomography (microCT)-based method for non-distorted semi-automated increment width detection; (2) calibrate physical and geochemical periodicity via vital staining and increment-resolved geochemical sampling; and (3) apply dynamic time warping (DTW) for chronological alignment of fragmented branch records. Applied to a single specimen (*Lithophyllum* sp.), this workflow yields the first composite sub-weekly to daily-resolved temperature reconstruction from a rhodolith and presents a multi-element temperature proxy for the Red Sea (Fig. 1).

Results

Rhodolith growth characterization and chronology

Linear extension was characterized in 21 fruticose thalli[43] (hereafter "branches" for brevity) of a free-living *Lithophyllum* sp. rhodolith (sample "AFE5"). It is important to note that the sampled branches occur on the outer living surface of the rhodolith. The rhodolith ($n = 1$) was stained with alizarin red prior to a four-month in-situ deployment on Al Fahal reef, a central Red Sea reef flat (13 March–23 July 2024; Fig. 1, Section "Sample selection, staining protocol, and identification"), providing a clear chronological marker for new skeletal accretion in each branch. Branches ($n = 21$) were deliberately sampled from all sides of the rhodolith, spanning multiple growth axes in different orientations, to capture changes in outer surface growth as the nodule rolls and reorients on the reef flat.

Growth among the 21 branches was highly heterogeneous, with linear extension ranging from 0.229 to 2.688 mm over the deployment interval (mean±: 1.42 ± .66 mm; Supplementary Table 1), encompassing more than a tenfold difference across branches from a single rhodolith. Growth rates measured here (mean ± SD: 10.77 ± 5.08/day; Supplementary Table 1) rank among the highest reported for rhodoliths in-situ[44,45]. Seven branches with the clearest stain lines and increments (defined in Section "MicroCT scanning, image and signal processing") were chosen for subsequent geochemical analysis. MicroCT imaging at 9–10 voxel size, selected as an optimal balance between spatial resolution, scanning time, and whole-branch coverage, enabled the consistent identification of growth increments (Section "MicroCT scanning, image and signal processing"). This was informed by preliminary scans at higher (4.5) and lower (35) resolutions (Fig. 2b, e), which demonstrated key tradeoffs between band order[46], noise, and volume of sample imaged. Manually measured increment width is highly variable and likely to be incomparable between two different observers as most increments do not have perfectly clear demarcations (Section "MicroCT scanning, image and signal processing"). Increment width was derived from density transects (Section "MicroCT scanning, image and signal processing"; Supplementary Fig. 2).

Single-branch proxy calibration

To characterize the thallus structure prior to destructive sampling, whole rhodoliths were first scanned by microCT to capture the three-dimensional morphology and internal density banding (Figs. 1a and 2). The best sample

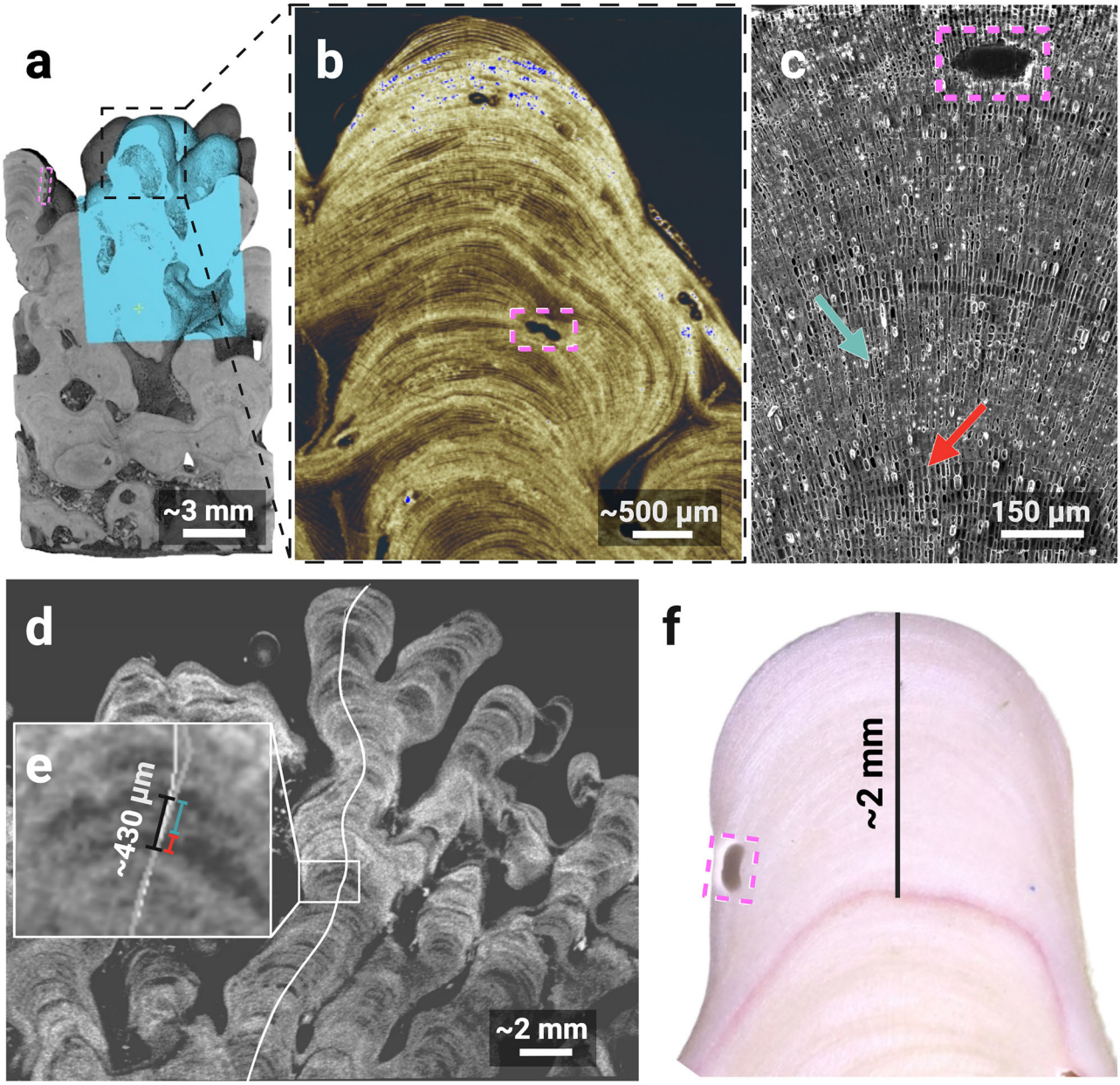

Fig. 2 | Multi-scale imaging characterization of rhodolith microstructure, growth banding, and seasonal cell variation. a Cored sample with high-resolution scan vision of interest (VOI) highlighted in blue. **b** Magnified portion of a showing 4.5 µm microCT scan, with lighter colors indicating higher density areas. Highest-density particles depicted in dark blue. Buried conceptacle visible in cross-section outlined in pink (see Section "Sample selection, staining protocol and identification"). **c** Scanning electron microscope (SEM) image taken using an Everhart–Thornley detector (ETD) at 20 kV and 0.13 nA with a working distance (WD) of 15 mm at 200× magnification showing seasonal variation in cell chambers. Longer, elongated cells are shown with the red arrow and shorter, denser cells are shown with the blue arrow. Buried conceptacle visible in cross-section outlined in pink. **d** MicroCT image (voxel size = 35 µm) in greyscale. Lighter colors correspond to higher density areas, and vice versa. White line (2.2 cm) showing path of curved slice, running perpendicular to growth axis. **e** Magnified portion of D showing banding (black), with lower density banding (red)and higher density banding (blue). **f** Light microscope image of sample (AFE5-2) stained with alizarin red. Between staining in spring (13 March 2024) and sample recovery in summer (23 July 2024), specimen grew ca. 2 mm.

was selected for further analyses (AFE5) on the basis of completeness and preservation. To address the potential heterogeneity of rhodolith growth, seven individual fruticose branches distributed across all axes of the rhodolith were subsampled (Fig. 3). For the purposes of this study, analysis was strictly limited to the linear extension of the living thallus tips accumulated during the 4-month post-staining experimental period, rather than the entire internal growth history. After scanning, branches were sectioned for increment-resolved geochemical analyses via laser ablation—inductively coupled plasma—mass spectrometry (LA-ICP-MS; see Section "Geochemical analyses") and density profiles via microCT scans (see Section "MicroCT scanning, image and signal processings") along the growth axes (Supplementary Fig. 1b and Fig. 3d). All single branch statistics (univariate/multivariate ordinary least squares (OLS) regressions and Monte Carlo uncertainty analysis across 17 molar element/Ca data; see Section "Geochemical analyses") were performed using AFE5-1 (growth ca. 1.8 mm).

Across the single-branch calibration (AFE5-1), only U/Ca and Ba/Ca show significant relationships with mean skeletal density, with both ratios higher in denser material (U/Ca: $r = 0.45$, $p = 0.00$; Ba/Ca: $r = 0.37$, $p = 0.02$). The correlation matrix further reveals a strong Li–alkali–Ba–Sr cluster (Li/Ca, Na/Ca, K/Ca, Sr/Ca, Ba/Ca) and a broader association of Fe/Ca, rare earth element ratios (La/Ca, Ce/Ca) and Pb/Ca with Sr/Ca and Ba/Ca, suggesting shared lattice-substitution or growth-related controls rather than

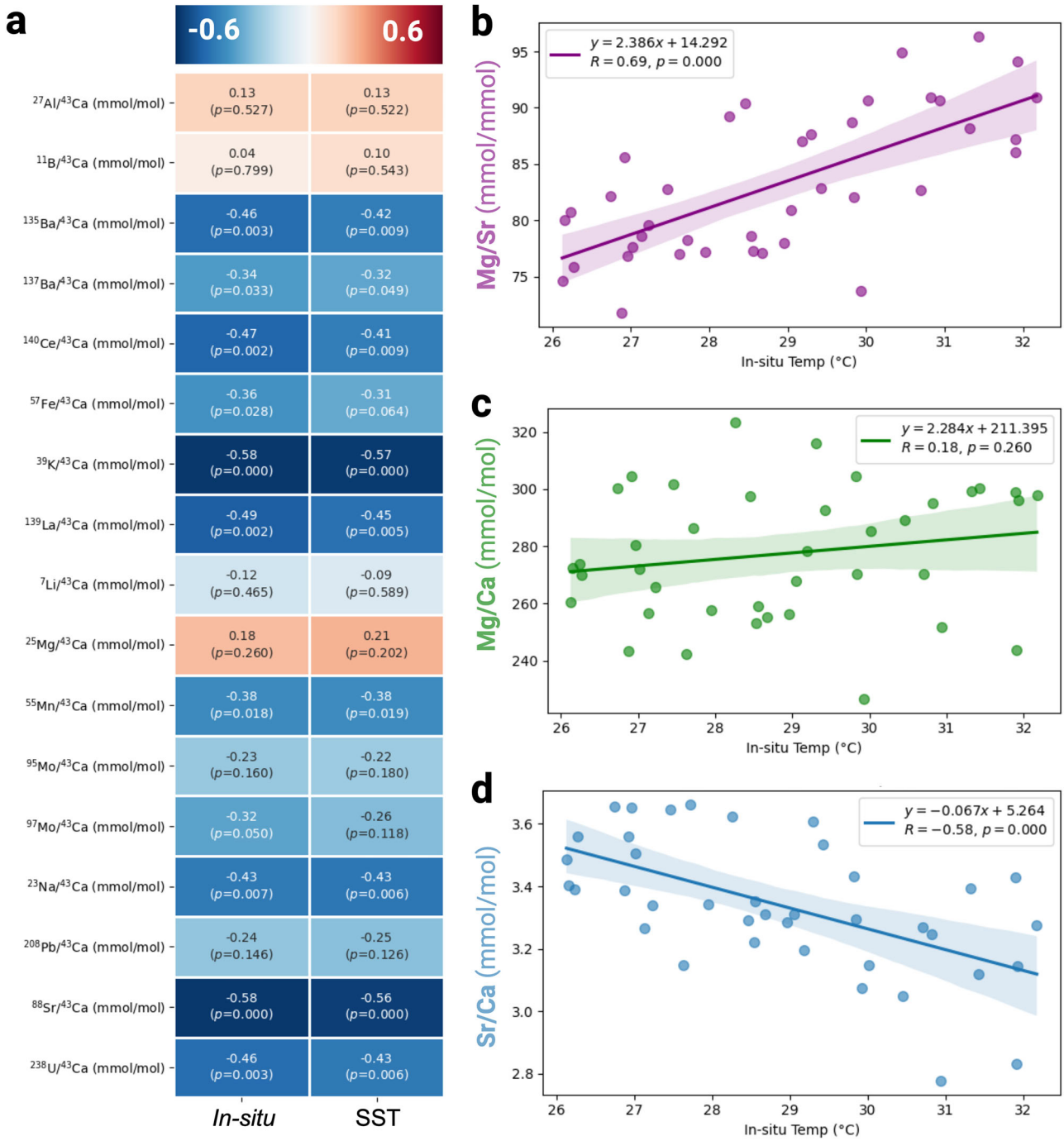

Fig. 3 | Single-branch proxy calibration against in-situ temperature. a Heatmap showing Pearson correlation coefficients (r) for 17 element/Ca data series from a single *Lithophyllum* sp. branch (AFE5-1) against daily in-situ temperature (left column) and satellite SST (right column) over the 133-day study period. Colors indicate correlation strength (red = positive, blue = negative), with p-values in parentheses. **b–d** Linear regression plots for the three primary temperature proxies against in-situ temperature: **b** Mg/Sr shows the strongest positive relationship ($r = 0.69$, $p < 0.001$), **c** Mg/Ca exhibits a weak, non-significant positive correlation ($r = 0.18$, $p = 0.26$), and **d** Sr/Ca displays a significant negative correlation ($r = -0.58$, $p < 0.001$). Shaded areas represent 95% confidence intervals for the regression lines. All geochemical data are from a single LA-ICP-MS transect on branch AFE5-1, aligned to the ARS anchor.

independent environmental forcing. Sr/Ca shows a significant negative correlation with temperature ($r = -0.58$, $p < 0.001$). While biogenic calcite typically exhibits a positive Sr/Ca–temperature relationship, negative relationships have been observed in inorganic calcite precipitation and may arise in biogenic systems where growth rate or calcification kinetics exert a dominant control on Sr incorporation. Derived extension rates (Section "Single-branch calibration and alignment with environmental data", Supplementary Note 1) correlate significantly with four ratios: Mg/Ca and B/Ca increase with growth rate (Mg/Ca: $r = 0.40$, $p = 0.01$; B/Ca: $r = 0.39$, $p = 0.01$), whereas Ba/Ca and U/Ca decrease (Ba/Ca: $r = -0.38$, $p = 0.02$; U/Ca: $r = -0.46$, $p = 0.00$), consistent with denser, slower-growing branches having elevated U/Ca and Ba/Ca. Several trace metals, including Al/Ca, are weakly or negatively correlated with most parameters and often close to detection limits, so these relationships should be interpreted cautiously.

Table 1 | Comparison of mean Pearson's correlation coefficients (*r*) and significance (*p*) for trace element ratios normalized to Calcium (Ca) versus Magnesium (Mg) against in-situ temperature (T_{IS})

Element	Mean Ca-normalized *r* (*p*)	Mean Mg-normalized *r* (*p*)	Δ*r*
Li	−0.34 (*0.21*)	−0.58 (*0.04*)	−0.21
Na	−0.24 (*0.38*)	−0.46 (*0.12*)	−0.22
Sr	−0.40 (*0.10*)	−0.58 (*0.07*)	−0.18
K	−0.27 (*0.10*)	−0.39 (*0.15*)	−0.12
Ba	−0.39 (*0.17*)	−0.43 (*0.21*)	−0.04
B	+0.15 (*0.40*)	−0.03 (*0.41*)	−0.18

Values represent the arithmetic mean across all analyzed *Lithophyllum* sp. branches ($n = 7$).

Multi-element normalization improves temperature proxy performance

In-situ temperatures were recorded to enable the comparison between element ratios and thermal variability using Hobo Pendant UA-64-001 loggers placed 1–2 m away from the cage site. The sensors, shaded beneath PVC covers to minimize solar heating effects[47], have an accuracy of ±0.54 °C and were calibrated against SBE-56 loggers. To evaluate the relationships between temperature and all measured elements, all possible cation-to-Ca ratios were systematically compared for their mathematical correlations with T_{IS} (Supplementary Fig. 3). This method identifies proxy combinations with the strongest correlations and most statistically significant associations with T_{IS} (Table 1). Pairwise Pearson correlations among cation-to-Ca ratios were calculated to assess covariance. Most elements co-varied positively, consistent with the expectation of shared geochemical controls (Sr–Mg: Pearson's $r = 0.42$). Correlations with ambient temperature are significantly improved by normalizing other element ratios by Mg/Ca, particularly Ba/Mg and Na/Mg, relative to traditional Ca-normalized proxies (Table 1). Normalizing element ratios to Mg consistently strengthened the correlation with temperature compared to traditional Ca-normalization, particularly for Sr, Li, and Na, suggesting that Mg is systematically involved in geochemical and/or biological processes.

In Mg/Sr-aligned regressions of all element/Ca ratios against in-situ temperature, several ratios (notably Sr/Ca, Ba/Ca, B/Ca, K/Ca, Li/Ca, and U/Ca) repeatedly explained a substantial fraction of temperature variance within individual branches (R^2 up to ~0.70), whereas other trace metals and rare earth element ratios showed weaker and less consistent relationships (Supplementary Table 2). These cross-branch patterns confirm that the strongest temperature sensitivity is concentrated in a limited subset of elements and further motivate the use of multi-element combinations rather than any single ratio alone.

Improving temperature reconstructions by aligning fruticose thalli growth records

To address the challenge of aligning incomplete and asynchronous geochemical records from multiple rhodolith branches, DTW was applied to the Mg/Sr time-series[48]. DTW aligns time-series flexibly by locally stretching or compressing sequences so that similar patterns can be compared (Fig. 4), even when sampling intervals vary[49]. A Sakoe–Chiba window constraint was implemented, limiting the warping path to ±30 days to prevent excessive or biologically unrealistic temporal distortions. Comparative analysis against unconstrained DTW demonstrated minimal differences in alignment cost and warping behavior across branches, indicating the constraint effectively regularizes alignment without impairing fit quality.

Fidelity analyses integrating Signal-to-Noise Ratio (SNR) and amplitude scaling revealed Mg/Sr more precisely isolates the temperature signal (SNR = 8.09) compared to Sr/Ca (SNR = 4.62). However, Sr/Ca exhibited larger relative amplitude changes (slope ratio 0.25) versus Mg/Sr's narrower range (0.0011). This reflects a tradeoff where Mg/Sr tracks fine-scale fluctuations tightly with reduced noise, whereas Sr/Ca captures broader variations accompanied by higher noise. Residual distributions further confirm Mg/Sr's reduced unexplained variance relative to Sr/Ca (Section "Alignment of rhodolith branche").

For the microCT-imaged branch AFE5-1, semi-automated increment trajectories increased the Mg/Sr–temperature fit from 41% explained variance under a linear time model to 49%, indicating that microCT-derived increment widths reduce chronological uncertainty for this branch. In contrast, branch AFE5-4 showed the strongest Mg/Sr–temperature relationship overall ($R^2 = 0.61$) using a simple linear time axis, outperforming AFE5-1 despite the absence of microCT-based increment information.

Discussion

The method proposed in this study allows the assembly of multiple fruticose thalli for an uninterrupted rhodolith growth record. Rhodoliths are some of the most prolific and resilient global marine archives[35,50]. Historically, they have been underutilized in paleoclimate research possibly due to their complex three-dimensional morphologies (Figs. 1a and 2d), disrupted growth banding and asynchronous branch extension (Fig. 4). The presented integrative workflow combines 3D microCT image processing (Fig. 2a, b, d, e; Section "MicroCT scanning, image and signal processing"), high-resolution geochemical time-series (Figs. 3 and 4; Section "Geochemical analyses") and DTW alignment (Fig. 4d; Section "Alignment of rhodolith branche") to address these obstacles, resulting in the first composite temperature reconstruction from a single rhodolith (Fig. 4) to the best of our knowledge.

Rhodolith chronologies achieve daily resolution comparable to tropical corals[7,51] and giant clams[52,53] and offer complementary advantages through resilience to marine heatwaves and ocean acidification[54,55]. As extreme environmental and climatic events increase in frequency and intensity, rhodoliths from regions of high thermal variability like the central Red Sea reef flats are strong contenders as dominant reef calcifiers. The highly convoluted, three-dimensional branching patterns of rhodoliths make traditional geological sectioning methods unsuitable for extracting growth and geochemical time-series (Fig. 2d). Arbitrary planar sectioning rarely aligns with the true growth axis, resulting in distorted measurements of increment width and density. Because each growth increment along the growth axis corresponds to a specific time of skeletal formation, any deviation from the longest axis introduces systematic error into the temporal framework, reducing the accuracy of climate reconstructions and comparisons. MicroCT scanning overcomes this limitation by providing non-destructive, high-resolution three-dimensional imaging of the entire specimen, allowing precise identification and extraction of the axis of maximal growth of each branch[56]. This ensures that measurements of increment width and density are accurate and undistorted, which is essential for meaningful interpretation of banding patterns and geochemical proxies.

Central to this workflow is the use of DTW for aligning asynchronous proxy records, a method well-suited for growth-variable series but accompanied by inherent challenges. Standard alignment approaches in corals, coralline algae, bivalves, trees, and speleothems often rely on visual or quantitative band counting, cross-dating, and modest interpolation or warping within an approximately linear age–distance framework. In contrast, fruticose rhodolith branches exhibit three-dimensional, asynchronous growth with frequent hiatuses and lateral bifurcation (Figs. 2d and 4), conditions under which simple linear interpolation or classical cross-dating alone are insufficient to recover a single, undistorted chronology. DTW is therefore used here as a quantitative extension of these concepts, allowing local stretching and compression so that geochemical data can be aligned even when sampling intervals and growth rates differ.

A critical consideration in any alignment-based reconstruction is the risk of overfitting, where an algorithm might force an artificial match to the target variable rather than recovering the true chronology. To minimize this risk, the DTW path was constrained by a Sakoe–Chiba band of 30 days anchored to the ARS line, preventing biologically implausible temporal shifts. Permutation tests further demonstrated that randomized data could not yield similarly high correlations, indicating that the observed fit is driven by the geochemical signal rather than by algorithmic forcing (Section

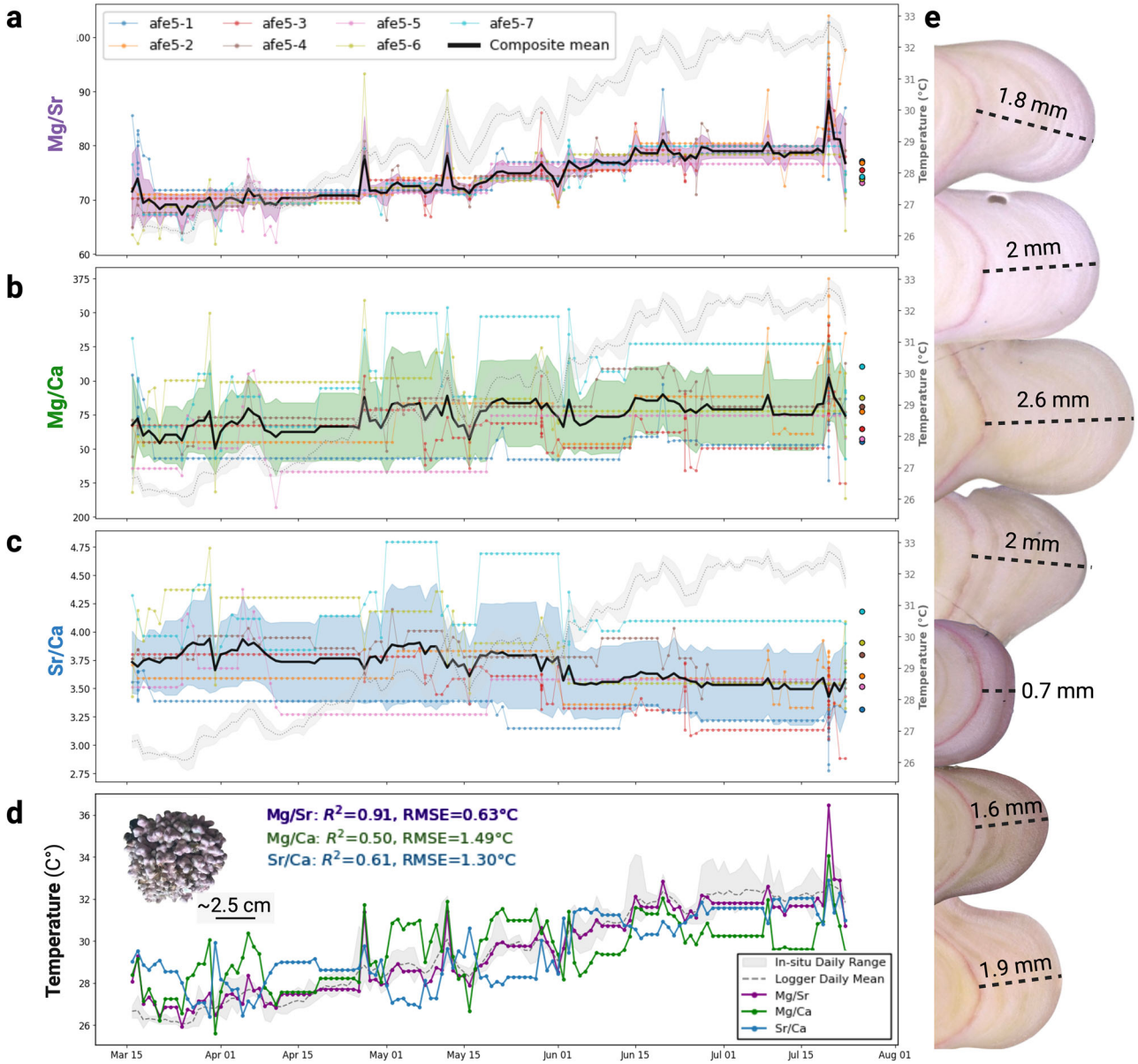

Fig. 4 | Reconstruction of seawater temperature using a multi-branch dynamic time warping (DTW) approach. a–c Temporal alignment of high-resolution geochemical proxies from seven individual rhodolith branches (colored lines/dots). Black line represents the composite mean of all DTW aligned branches, with shaded regions indicating ±1 SD. Proxies shown are **a** Mg/Sr, **b** Mg/Ca, and **c** Sr/Ca. The background grey dashed line and shading represent the daily mean and range of in-situ logger temperatures, respectively. Right panels show cross-sections of the corresponding rhodolith branches with total growth extension indicated (dashed lines). **d** Final calibration of the composite proxy data against in-situ temperature. The reconstructed temperatures (solid lines) derived from the composite Mg/Sr (purple), Mg/Ca (green), and Sr/Ca (blue) records are plotted against the observed logger temperature (grey dashed line). Mg/Sr: R^2 = 0.91, RMSE = 0.63 °C; Sr/Ca: R^2 = 0.61, RMSE = 1.3 °C; Mg/Ca: R^2 = 0.51, RMSE = 1.5 °C. **e** Light microscopy images of rhodolith branches selected for geochemical sampling. Black dashed line indicates linear extension over the study interval, spanning from the alizarin red stain front to the last living tissue.

"Alignment of rhodolith branche"). Most importantly, the final composite proxy is derived from the arithmetic mean of seven independently aligned branches, such that any alignment driven primarily by noise would tend to average out. Instead, the multi-branch integration yields a coherent signal (R^2 = 0.91) that substantially exceeds even the best single-branch record (R^2 = 0.61).

To optimize proxy fidelity, all possible element-to-element ratios have been evaluated. Although trace-element abundances are initially quantified relative to Ca (as an internal standard), the strongest and most robust temperature relationship emerged for Mg/Sr (i.e., (Mg/Ca)/(Sr/Ca), so the Ca term effectively cancels). This specific pairing appears to leverage the complementary thermodynamic behaviors of the two ions: endothermic incorporation of Mg[57] records temperature, though it is obscured by biological effects (unknown "vital effects"), whereas Sr incorporation is more kinetically controlled and sensitive to precipitation rate[58]. By ratioing the two (Mg/Sr), the thermal signal (Mg) is effectively normalized by the growth rate signal (Sr). This "temperature-to-growth" normalization minimizes the high-frequency kinetic noise that typically obscures single-element records. Empirically, this ratio linearizes the proxy response, yielding a composite reconstruction with an RMSE (0.63 °C) comparable to instrumental precision (0.54 °C).

This study demonstrates that multi-branch proxy composites markedly improve temperature reconstruction accuracy. By integrating microCT imaging, vital-stain calibration, and DTW assembly, we show that multi-branch proxy composites markedly improve temperature reconstruction accuracy. Future work extending this approach across multiple specimens

and regions will unlock the full potential of rhodolith archives for high-resolution paleoclimate reconstructions. By enabling sub-seasonal to daily reconstructions from a previously inaccessible global archive, this workflow expands the paleoclimate toolkit, especially as traditional archives like corals and mollusks are increasingly threatened. High-resolution, biologically informed records from resilient taxa are critical for resolving fine-scale temperature variability[59], which directly affects coral bleaching frequency, carbonate production, and ecosystem resilience[60].

This methodological framework (Section 6) also has potential utility beyond rhodoliths for archives characterized by inherent discontinuities or asynchronous growth, such as speleothems or multi-archive datasets requiring integration of records formed at varying rates and time-scales. This study thus broadens both the geographic and temporal scope of high-quality paleotemperature records and enhances the ability to anticipate tropical reef responses to ongoing and future ocean warming.

Methods

Sample selection, staining protocol, and identification

To calibrate growth periodicity, skeletal density and element incorporation patterns, rhodoliths were collected from ~1 m water depth by snorkelers around midday on 6 March 2024 from the exposed side of Al Fahal (22°17'51.37"N, 038°57'43.90"E) (Fig. 1c), a midshore reef flat within the Shib Nazar reef system, which contains several reef flats (0.5–1.5 m) within 10 km of each other[41]. Samples were selected based on gross morphology and excluded if fouled by macroalgae. After collection, samples were transported in seawater-filled coolers and maintained under ambient conditions in the Coastal Marine Resources Core lab aquaria at King Abdullah University of Science and Technology (KAUST).

Following a one-week acclimation in outdoor flow-through tanks, rhodoliths were stained over a 60-h time interval with 85 mg/L alizarin red[61,62]. Stained rhodoliths were deployed on 15 March 2024 in two custom-built plastic mesh cages (mesh size: ~2.5 cm) (Supplementary Fig. 1a). Cages were designed to allow for water flow and rolling, in the interest of preserving natural growth conditions and were cleaned every 2 to 3 months to mitigate fouling and preserve ambient light and water exposure. For calibration and to constrain seasonal growth differences, a subset of randomly selected samples was retrieved after approximately four months (23 July 2024).

For light microscopy, microCT scanning, scanning electron microscopy (SEM), and LA-ICP-MS, samples were air-dried, and branches from all axes of the rhodolith were broken off with a chisel. Branches were embedded lengthwise in 1-inch diameter epoxy stubs, polished with 1 µm Al_2O_3 powder, and imaged under a stereomicroscope. Growth was measured in ImageJ[63] by identifying stained bands and quantifying linear extension from the stained margin (Fig. 4d).

Recent studies demonstrate that site- and species-specific calibrations are essential for coralline algal proxy development, but cryptic diversity and morphological plasticity complicate species identifications[64,65]. SEM identification to *Lithophyllum* sp. was based on presence of diagnostic buried uniporate conceptacles, secondary pit connections[66] (see Fig. 2, pink boxes in b, c, f), and the absence of visibly retained epithallial cells, a diagnostic feature of *Titanoderma* sp[67]. SEM imaging was performed using an Everhart–Thornley detector (ETD) at 20 kV accelerating voltage, 0.13 nA beam current, and 10–15 mm working distance to visualize seasonal variation in cell chamber size (200× magnification; Fig. 2c) and ultrastructural features (15,000× magnification). Monospecificity within a single individual was confirmed by microCT, with no evidence of partial die-off or secondary colonization. Geochemical calibrations were performed on all branches from a monospecific individual (AFE5; Fig. 2f, 5), and the most continuously growing branch was selected and applied to the full dataset.

Individual growth periodicity, skeletal density, and incorporation of major and minor elements into the skeleton were calibrated by reconstructing the full growth history from 13 March to 23 July 2024, using seven branches (see Fig. 4d). Whereas the single-individual approach limits the generalizability of our specific proxy calibrations, it demonstrates methodological feasibility. Broader population or regional studies would require species-level identification to account for cryptic diversity and provide a comprehensive population-level calibration in Lithophylloideae and coralline algae in general.

MicroCT scanning, image, and signal processing

Rhodolith sample AFE5-1 was microCT scanned whole to generate a 3D densitometry map for or assessment of internal structure, monospecificity, and potential diagenetic alteration. A high-resolution microCT scan was available for a single branch (AFE5-1), from which semi-automated increment width trajectories were derived and used to construct a physically informed time axis for the laser transect. Scans were performed at the University of Barcelona CORELAB using a MultiTom Core system with a 1 mm Al filter, 150 kV, 30 W, 1500 projections, and 12 averages to optimize scanning time, resolution, and sample coverage.

MicroCT scans were reconstructed into 3D volumes using TESCAN's Acquila software[68] and exported as Avizo™ files. All image analysis was completed using the Visualization Core Lab facilities at KAUST. Scans were visualized in ThermoFisher Scientific Avizo™ (RRID:SCR_014431) software and thresholded to optimize visibility of the density banding. Using Avizo™, samples were rendered as volumes, and suitable branches were selected based on length, clarity of banding, and completeness. To ensure that the most comprehensive view of the growth history of each sample was obtained, branches from as many different growth axes as possible were selected within the limitations of each scan.

After finding a suitable cross-section through AFE5-1, a transect was plotted through the center of the branch using the apex of the density bands as a guide with "Curved Slice" at the finest resolution (Supplementary Fig. 1b). Multiple curved slices were plotted onto the same branch to ensure that the transect ran fully perpendicular to the growth axis. All 3D image processing was completed using ThermoFisher Scientific Avizo™.

Growth increments within rhodolith branches were experimentally resolved using microCT scans at multiple voxel resolutions, revealing a hierarchical structure of skeletal accretion bands at different spatial scales. At the finest resolution (~4.5 µm voxel size), ultrafine increments potentially representing sub-daily or diurnal microbands were visible, though these scans include fine-scale textural variability potentially considered biological or mineralogical noise, and were not interpretable (Fig. 3b). Intermediate resolution scans at 9–10 µm voxel size captured clearer growth increments, providing an optimal balance between spatial detail and noise reduction. Coarser imaging at 35 µm voxel size resolved larger "bundled" increments aggregating multiple bands, representing approximately weekly to monthly growth increments (Fig. 2d, e). The lowest resolution scans at 80 µm (Fig. 1a) visualized overall branch morphology and gross density variations but did not resolve discrete growth increments suitable for temporal calibration. This multi-resolution imaging framework allowed precise identification and calibration of growth increments, enabling temporally resolved geochemical sampling.

Using the same transect from the "Curved Slice", the gray scale values were extracted from the microCT scan to get a measure of relative derived skeletal density perpendicular to the growth axis using "Line Set Probe" in Avizo™ imaging software. All resulting probes from "Line Set Probe" were standardized by subtracting the mean and dividing by the standard deviation to ensure comparability, as the relative values of density are not directly comparable between scans taken with different tube settings[69] (see Section "MicroCT scanning, image and signal processing").

Manual measurement of growth increment widths in rhodolith branches is highly dependent on the surveyor's semi-arbitrary judgment of where band boundaries lie, resulting in substantial variability even within repeated measurements of the same specimen over different days. This variability raises significant concerns regarding reproducibility and objectivity (see Fig. 2b, d, e for examples). To quantify differences in surveyor biases in increment measurements, the proportion of increment boundaries, or demarcations between density bands, identified by each observer that were not matched by the other was calculated.

To overcome these limitations, an objective, quantitative method was developed (Supplementary Fig. 2). Several density transects (using "Curved Slice" and "Line Set Probe", see Supplementary Fig. 1c) were extracted from the microCT scans using Avizo™ image processing. To reduce noise, the data were smoothed using a Savitzky–Golay filter (window length = 11, polynomial order 2)[70]. Peaks and valleys representing growth band extrema were identified using the SciPy'find_peaks' function[71], applying tuned parameters for minimum distance and prominence to isolate significant features. Derived increments were computed as distances between successive extrema, and local maxima/minima were located where the derivative crosses 0. Concurrently, manual increment widths were measured and increment positions calculated by cumulative summation. To compare datasets, derived increments were interpolated to manual increment positions, enabling regression analysis. To account for possible nonlinear temporal distortions, DTW was implemented for alignment prior to further regression. The computational workflow, including smoothing, peak detection, alignment, regression, and visualization was performed using Python.

Geochemical analyses

Major and minor element concentrations were measured in individual rhodolith branches ($n = 7$) using LA-ICP-MS at the Max Planck Institute for Chemistry (Mainz, Germany). All analyses were performed with a solid-state New Wave UP-213 laser system (213 nm) coupled to a single-collector sector-field Thermo Fisher Scientific ELEMENT2 mass spectrometer. Laser spots ($n = 320$ total; 40 diameter) were measured across each selected rhodolith branch. Spots were placed along the apex of each visible band, following the growth axis of each branch. Ablation transects began at the last living tissue and extended to the apex of the stained band. Each spot was ablated with a laser energy of ~9 J/cm², a 15-s warm-up, 45-s well time, and 30-s washout between spots. LA-ICP-MS was used to measure the abundance of ^{7}Li, ^{11}B, ^{23}Na, ^{25}Mg, ^{27}Al, ^{39}K, ^{55}Mn, ^{57}Fe, ^{88}Sr, ^{95}Mo, ^{97}Mo, ^{135}Ba, ^{137}Ba, ^{139}La, ^{140}Ce, ^{208}Pb, and ^{238}U. All trace element ratios are reported normalized to ^{43}Ca.

Calibration was performed using the NIST SRM 612 silicate glass reference material (National Institute of Standards and Technology), which is homogeneous at the nanometer to micrometer scale for many elements, though its silicate matrix differs from that of calcium carbonate. The MACS-3 pressed powder pellet (USGS), with certified mass fractions of Mg = 1756 µg/g and Ca = 37.69% m/m, was used as a quality control reference material. Both NIST SRM 612 and MACS-3 were measured at the beginning and end of each analytical session and additionally every 80–100 sample measurements, to ensure analytical accuracy and precision throughout the run. Data were reduced using an in-house software program following established reduction equations[72,73].

Environmental data processing

Hourly in-situ temperature data were recorded for the full study interval (13 March–23 July 2024). These data were recorded using Hobo Pendant UA-64-001 loggers (deployed 1–2 m from cage site) with an accuracy of 0.54 °C, shaded under PVC to reduce solar bias[47] and calibrated against SBE-56 loggers. Daily mean sea surface salinity (SSS) data were downloaded from CoastWatch Level-3 SSS (http://coastwatch.noaa.gov/cwn/), generated from NASA Jet Propulsion Laboratory Soil Moisture Active Passive satellite observations of the ocean for the closest available coordinates to the study site.

Single-branch calibration and alignment with environmental data

It is important to note that averaging linear regression statistics across seven distinct branches (Table 1) inherently dampens the strength of the recorded signal. Because rhodolith branches grow at different rates and directions, their individual time-series are not perfectly aligned in this linear-age model, leading to phase shifts that obscure the true fidelity of the proxy when aggregated as a simple mean. Consequently, the mean correlations presented in Table 1 represent a conservative lower bound of proxy fidelity. The raw linear alignment does not account for non-linear growth pauses. Despite this blurring, the systematic improvement of Mg-normalized ratios suggests a robust underlying thermodynamic control.

For all branches, a simple linear time model that distributes analytical spots evenly between deployment and retrieval dates was therefore considered as a baseline. In addition, an increment-resolved time model was developed for the microCT-imaged branch (AFE5-1) and evaluated in parallel. For each branch and available time model, Mg/Sr was calibrated against in-situ temperature, and the combination that maximized R^2 was selected as the candidate transfer function for construction of the Mg/Sr reference template, to which all branches were subsequently aligned using DTW (Section 6). An additional set of regressions between these element/Ca ratios and SSS yielded no statistically significant relationships and thus are not reported in detail. Although Al/Ca showed an apparent correlation with SSS, this was based on a small number of measurements close to the analytical detection limit and is therefore considered spurious and not discussed further.

Accounting for seasonal growth rate variability is crucial for precise calibration of high-resolution proxy data[74], as overlooking this can lead to temporal misalignment with environmental records and bias results toward intervals of rapid growth. Growth rates for AFE5-1 were estimated by combining microCT-derived skeletal density profiles with the time elapsed between staining and collection (13–15 March to 23 July 2024). Each branch's growth axis was divided into increments defined by visible growth bands (9–10 µm voxel size), and the spatial position of each increment was converted to elapsed time by proportionally distributing the total growth period according to the density profile, assuming that lower-density areas correspond to elongated cell chambers (Fig. 2c, e) and therefore faster extension[75] (for a more detailed explanation of growth rate scaling, refer to Supplementary Note 1). Growth rates (µm day^{-1}) were then calculated by dividing increment widths by their assigned time intervals (Supplementary Table 1). It should be noted that this approach provides an approximation that may oversimplify the complex growth dynamics of rhodoliths.

Each increment was assigned a unique timestamp, derived from the growth rate model, which links its position along the branch (distance) to a specific point in time. This timestamp enables direct alignment of increment-resolved data with both time-based (i.e., temperature, salinity) and distance-based (i.e., element chemistry, density) datasets. Growth rate curves from multiple branches were averaged to produce a composite, density-weighted growth history with time as the independent variable (Supplementary Fig. 1c). Using the timestamps derived from the growth rate model, skeletal density, growth rate, temperature, salinity, and geochemical data were temporally aligned and binned for each increment. For every increment, all corresponding data within its spatial boundaries were extracted, and mean values for each parameter were calculated. The resulting dataset includes, for each increment, its position, mean skeletal density, growth rate, temperature, salinity, elemental concentration, and a representative timestamp. This approach enables high-resolution, time-resolved integration of physical, geochemical, and environmental data, allowing for precise calibration and interpretation of rhodolith growth records.

In the present dataset, only branch AFE5-1 was available for microCT-based increment modelling, whereas the remaining branches were constrained to the linear time model. Despite the improved local Mg/Sr–temperature fit for AFE5-1 obtained using curve-based microCT time axes, the most continuously growing branch (AFE5-4) under the linear model provided the strongest Mg/Sr–temperature relationship and therefore served as the basis for the synthetic master used in subsequent DTW and composite calibration.

Alignment of rhodolith branches

To address the challenge of incomplete and asynchronous growth among individual rhodolith branches, a calculated reference template was used. First, the relationship between molar Sr/Ca and temperature was calibrated using the branch with the most complete chronology and best-resolved

growth increments. Mg/Sr in branch AFE5-4 was selected as the reference ratio for alignment because it showed the strongest predictive relationship with temperature despite the linear temporal assumption, which is fundamentally flawed. Using this calibration equation and the observed temperature record, a continuous reference template of predicted Mg/Sr values was generated for the duration of post-stain growth.

Measured Mg/Ca, Sr/Ca, and Mg/Sr time-series from each branch were then aligned to the reference template using DTW[76]. DTW matches the proxy record of each branch to the template, accounting for differences in growth rate, gaps in the chronology, and overall record length (Fig. 4d). Each measured data point was mapped to an estimated date on the reference timeline (Fig. 4a–d). Only the actual measured values from each branch were used in the final composite; the template values themselves were not included in the compiled record. The integrated growth history was constructed by averaging the aligned measured values from all branches at each point on the reference timeline (Fig. 2a, b). Linear regressions of proxies to temperature were performed to estimate the SNR, defined as the variance explained by temperature divided by residual variance. Residual time-series and distributions were analyzed to evaluate the magnitude and pattern of unexplained variance.

Overfitting tests and statistical analyses

To ensure the multi-branch composite reconstruction represents a genuine climate signal rather than aliasing introduced by DTW alignment forcing spurious correspondence between proxy and temperature series, three rigorous controls against overfitting were implemented. First, the DTW algorithm was constrained using a Sakoe–Chiba band of ±30 days, preventing biologically unrealistic temporal distortions. This window accommodates natural growth pauses[38] while prohibiting the algorithm from forcing alignment between disparate seasonal regimes. Second, a permutation test ($n = 1000$) was performed to quantify the probability of obtaining the composite correlation by chance. Null distributions were generated by randomly shuffling the time-series blocks (block length = 7 days) of the predictor variables while preserving their autocorrelation structure. The observed composite correlation ($R^2 = 0.91$) far exceeds the 95th percentile of the null distribution (R^2 null 95% = 0.18, $p < 0.001$), providing evidence that the alignment is driven by a shared environmental signal. Third, the composite was validated against a flat-master control. Alignment of branches to a synthetic constant-growth master (assuming constant linear extension) yielded a significantly lower correlation ($R^2 = 0.31$) compared to the DTW-aligned composite ($R^2 = 0.91$). This demonstrates that the high fidelity of the reconstruction is not an inherent property of the raw geochemical data but rather a result of resolving the non-linear growth history shared across branches through DTW.

Collinearity was assessed using correlation matrices and variance inflation factors (VIF). Mean growth rate and mean density were perfectly (negatively) correlated ($r = -1.00$, VIF > 300) because growth rate was directly derived from density; only one was included in any model. Other predictors were checked for collinearity (|R| <0.7), and highly correlated pairs were not used together.

Univariate and multivariate OLS regressions were performed to relate element ratios to mean temperature, growth rate (or density), and increment width:

$$y = \beta_0 + \beta_1 x_1 + \beta_2 x_2 + \beta_3 x_3 + \varepsilon$$

where y is the elemental ratio, x_1 is mean temperature, x_2 is mean growth rate (or density), x_3 is increment width, and ε is the error term. Model assumptions (linearity, independence, homoscedasticity, normality) were checked visually and statistically. To control for the increased risk of Type I errors from multiple statistical tests, the Benjamini–Hochberg procedure[77] was applied to adjust p-values and maintain a false discovery rate below 0.05. To test robustness to measurement uncertainty, 1000 Monte Carlo simulations were run per model (each element ratio—temperature correlation, see Fig. 3a or Section "Geochemical analyses" for full list), adding Gaussian noise to temperature based on empirical error estimates. Regression outputs were summarized as mean ± confidence intervals.

Data availability

Geochemical data from sample AFE5 (branches 1–7), microCT density transects, and daily mean in-situ temperature data are archived and accessible at Dryad Data Repository (https://doi.org/10.5061/dryad.h1893201z).

Code availability

Code for reproducing DTW analysis is available on GitHub at https://github.com/lenayueshali/Rhodo-pipeline.

Received: 8 October 2025; Accepted: 1 May 2026;
Published online: 21 May 2026

References

1. Hughes, T. P., Baird, A. H., Morrison, T. H. & Torda, G. Principles for coral reef restoration in the Anthropocene. *One Earth* **6**, 656–665 (2023).
2. Reaka-Kudla, M. L. The global biodiversity of coral reefs: a comparison with rainforests. In *Biodiversity II: Understanding and Protecting Our Natural Resources* (eds Reaka-Kudla, M. L. et al.) 83–108 (National Academy Press, Washington, D.C., 1997).
3. Hughes, T. P. et al. Global warming transforms coral reef assemblages. *Nature* **556**, 492–496 (2018).
4. Drury, C. Resilience in reef-building corals: the ecological and evolutionary importance of the host response to thermal stress. *Mol. Ecol.* **29**, 448–465 (2019).
5. Bos, J. T. & Pinsky, M. L. Fine resolution satellite sea surface temperatures capture the conditions experienced by corals at monthly but not daily timescales. *Coral Reefs* **44**, 423–434 (2025).
6. Safaie, A. et al. High frequency temperature variability reduces the risk of coral bleaching. *Nat Commun* **9**, 1671 (2018).
7. Murty, S. A. et al. Spatial and temporal robustness of Sr/Ca-SST calibrations in Red Sea corals: evidence for influence of mean annual temperature on calibration slopes. *Paleoceanogr. Paleoclimatol.* **33**, 443–456 (2018).
8. Cohen, A. L. & McConnaughey, T. A. Geochemical perspectives on coral mineralization. *Rev. Mineral. Geochem.* **54**, 151–187 (2003).
9. Kodama, S. et al. Carbon and oxygen isotope records of *Tridacna squamosa* shells from two different latitudes in the Ryukyu Islands. *Paleontological Research* **25**, 79–92 (2021).
10. Schöne, B. et al. Daily growth rates in shells of *Arctica islandica*: assessing sub-seasonal environmental controls on a long-lived bivalve mollusk. *Palaios* **20**, 78–92 (2005).
11. Öğretmen, N., Angulo-Preckler, C., Aranda, M., Duate, C. M. & Westphal, H. The northern Red Sea (Shushah Island) coral health inferred from benthic foraminifers. *Diversity* **16**, 463 (2024).
12. Reiss, Z. & Hottinger, L. The gulf of aqaba: ecological micropaleontology. In *Ecological Studies*, Vol, 50, 354 (Springer-Verlag, 1984).
13. Urey, H. C., Lowenstam, H. A., Epstein, S. & McKinney, C. R. Measurement of paleotemperatures and temperatures of the Upper Cretaceous of England, Denmark, and the southeastern United States. *Bull. Geol. Soc. Amer.* **62**, 399–416 (1951).
14. Masanja, F. et al. Impacts of marine heat extremes on bivalves. *Front. Mar. Sci.* **10**, 1159261 (2023).
15. Schoepf, V. et al. Corals at the edge of environmental limits: a new conceptual framework to re-define marginal and extreme coral communities. *Sci. Total Environ.* **884**, 163688 (2023).
16. Schöne, B. R. The curse of physiology—challenges and opportunities in the interpretation of geochemical data from mollusk shells. *Geo-Mar. Lett.* **28**, 269–285 (2008).

17. Amado-Filho, G. M., Bahia, R. G., Pereira-Filho, G. H. & Longo, L. L. South Atlantic rhodolith beds: latitudinal distribution, species composition, structure and ecosystem functions, threats and conservation status. In *Rhodolith/Maërl Beds: A Global Perspective* (eds Riosmena-Rodríguez, R. et al.) 299–317 (Springer International Publishing, 2017).
18. Brasileiro, P. S. et al. Macroalgal composition and community structure of the largest rhodolith beds in the world. *Mar. Biodivers.* **46**, 407–420 (2015).
19. Littler, M. M., Littler, D. S., Blair, S. M. & Norris, J. N. Deepest known plant life discovered on an uncharted seamount. *Science* **227**, 57–59 (1985).
20. Adey, W. H. & Macintyre, I. G. Crustose coralline algae: a re-evaluation in the geological sciences. *Geol. Soc. Am. Bull.* **84**, 883–904 (1973).
21. Kamenos, N. A., Cusack, M. & Moore, P. G. Coralline algae are global palaeothermometers with bi-weekly resolution. *Geochim. Cosmochim. Acta* **72**, 771–779 (2008).
22. Kamenos, N. A., Burdett, H. L. & Darrenougue, N. Coralline algae as recorders of past climatic and environmental conditions. In *Rhodolith/Maërl Beds: A Global Perspective* (eds Riosmena-Rodríguez, R. et al.) 27–53 (Springer, 2017).
23. MacDonald, E. et al. Timing of calcification and environmental variability determine pH proxy fidelity in coastal calcifying macroalgae. *Limnol. Oceanogr.* **70**, 2733–2744 (2025).
24. McCoy, S. J. & Kamenos, N. A. Coralline algae (Rhodophyta) in a changing world: integrating ecological, physiological, and geochemical responses to global change. *J. Phycol.* **51**, 6–24 (2015).
25. Halfar, J., Zack, T., Kronz, A. & Zachos, J. C. Growth and high-resolution paleoenvironmental signals of rhodoliths (coralline red algae): a new biogenic archive. *J. Geophys. Res.* **105**, 22107–22116 (2000).
26. Frantz, B. R., Kashgarian, M., Coale, K. H. & Foster, M. S. Growth rate and potential climate record from a rhodolith using ^{14}C accelerator mass spectrometry. *Limnol. Oceanogr.* **45**, 1773–1777 (2000).
27. Hetzinger, S. et al. Reproducibility of *Clathromorphum compactum* coralline algal Mg/Ca ratios and comparison to high-resolution sea surface temperature data. *Geochim. Cosmochim. Acta* **220**, 96–109 (2018).
28. Light, T. et al. Advancing Mg/Ca analysis of coralline algae as a climate proxy by assessing LA-ICP-OES sampling and coupled Mg/Ca-$\delta^{18}O$ analysis. *Geochem. Geophys. Geosyst.* **19**, 2876–2894 (2018).
29. Kamenos, N. & Law, A. Temperature controls on coralline algal skeletal growth. *J Phycol.* **46**, 331–335 (2010).
30. Caragnano, A. et al. The coralline red alga *Lithophyllum kotschyanum* f. affine as proxy of climate variability in the Yemen coast, Gulf of Aden (NW Indian Ocean). *Geochim. Cosmochim. Acta* **124**, 1–17 (2014).
31. Darrenougue, N., De Deckker, P., Eggins, S. & Payri, C. Sea-surface temperature reconstruction from trace elements variations of tropical coralline red algae. *Quat. Sci. Rev.* **93**, 34–46 (2014).
32. Tuya, F. et al. Levelling-up rhodolith-bed science to address global-scale conservation challenges. *Sci. Total Environ.* **892**, 164818 (2023).
33. Schils, T. Branching *Lithophyllum* coralline algae: dominant reef builders on herbivory-depressed tropical reefs after high coral mortality. *Diversity* **15**, 1025 (2023).
34. Gomez-Lemos, L. A. & Diaz-Pulido, G. Crustose coralline algae and associated microbial biofilms deter seaweed settlement on coral reefs. *Coral Reefs* **36**, 453–462 (2017).
35. Burdett, H. L. et al. Dynamic photoinhibition exhibited by red coralline algae in the Red Sea. *BMC Plant Biol.* **14**, 139 (2014).
36. Williams, S. et al. Reprint of: Comparison of climate signals obtained from encrusting and free-living rhodolith coralline algae. *Chem. Geol.* **526**, 175–185 (2019).
37. Halfar, J. et al. Coralline algal growth-increment widths archive North Atlantic climate variability. *Palaeogeogr. Palaeoclimatol. Palaeoecol.* **302**, 71–80 (2011).
38. Sletten, H. R., Andrus, C. F. T., Guzmán, H. M. & Halfar, J. Re-evaluation of using rhodolith growth patterns for paleoenvironmental reconstruction: an example from the Gulf of Panama. *Palaeogeogr. Palaeoclimatol. Palaeoecol.* **465**, 264–277 (2017).
39. Berumen, M. et al. The Red Sea: environmental gradients shape a natural laboratory in a nascent ocean. In *The Red Sea* (eds Duarte, C. M. & Voolstra, C. R.) (Springer, 2019).
40. Sanikommu, S. et al. Making the case for high-resolution regional ocean reanalyses: an example with the Red Sea. *Bull. Amer. Meteor. Soc.* **104**, E1241–E1264 (2023).
41. Rich, W. A., Carvalho, S. & Berumen, M. L. Coral bleaching due to cold stress on a central Red Sea reef flat. *Ecol. Evol.* **12**, e9450 (2022).
42. Osman, E. O. et al. Thermal refugia against coral bleaching throughout the northern Red Sea. *Glob. Change Biol.* **24**, e474–e484 (2018).
43. Woelkerling, W. J., Irvine, L. M. & Harvey, A. S. Growth-forms in non-geniculate coralline red algae (Corallinales, Rhodophyta). *Aust. Syst. Bot.* **6**, 277–293 (1993).
44. Steller, D., Hernandez-Ayón, J., Riosmena-Rodríguez, R. & Cabello-Pasini, A. Effect of temperature on photosynthesis, growth and calcification rates of the free-living coralline alga *Lithophyllum margaritae*. *Cienc. Mar.* **33**, 441–456 (2007).
45. Adey, W. H. & McKibbin, D. L. Studies on the maerl species *Phymatolithon calcareum* (Pallas) nov. comb. and *Lithothamnium coralloides* Crouan in the Ria de Vigo. *Bot. Mar.* **12**, 100–106 (1970).
46. Chan, P. et al. Micro-computed tomography: applications for high-resolution skeletal density determinations. An example using annually banded crustose coralline algae. *Geochem. Geophys. Geosyst.* **18**, 3781–3800 (2017).
47. Rich, W. et al. Widespread inconsistency in logger deployment methods in coral reef studies may bias perceptions of thermal regimes. *PLoS Clim.* **3**, e0000517 (2024).
48. Sakoe, H. & Chiba, S. Dynamic programming algorithm optimization for spoken word recognition. *IEEE Trans. Acoust. Speech Signal Process.* **26**, 43–49 (1978).
49. Krotov, A. et al. Time-warping analysis for biological signals: methodology and application. *Sci. Rep.* **15**, 11718 (2025).
50. Krieger, E. C. et al. Tolerance of coralline algae to ocean warming and marine heatwaves. *PLoS Clim.* **2**, e0000092 (2023).
51. Sinclair, D. J., Williams, B. & Risk, M. A biological origin for climate signals in corals: trace element "vital effects" are ubiquitous in scleractinian coral skeletons. *Geophys. Res. Lett.* **33**, L17707 (2006).
52. Brosset, C. et al. Integrating high-resolution Sr/Ca and ultrastructural analyses of the *Tridacna squamosa* shell to reconstruct sub-daily seawater temperature variation. *Palaeogeogr. Palaeoclimatol. Palaeoecol.* **659**, 112663 (2025).
53. Yan, H. Daily growth bands of giant clam shell: a potential paleoweather recorder. *Solid Earth Sci.* **5**, 249–253 (2020).
54. Nannini, M. et al. Withstanding the heat: resilience of free-living coralline algae to marine heatwaves. *Mar. Environ. Res.* **212**, 107538 (2025).
55. Schubert, N. et al. Calcification in free-living coralline algae is strongly influenced by morphology: implications for susceptibility to ocean acidification. *Sci. Rep.* **11**, 11232 (2021).
56. Nitsch, F., Nebelsick, J. H. & Bassi, D. Constructional and destructional patterns—void classification of rhodoliths from Giglio Island, Italy. *Palaios* **30**, 680–691 (2015).
57. Moberly, R. Jr. Composition of magnesian calcites of algae and pelecypods by electron microprobe analysis. *Sedimentology* **11**, 61–82 (1968).
58. Gabitov, R. I., Sadekov, A. & Leinweber, A. Crystal growth rate effect on Mg/Ca and Sr/Ca partitioning between calcite and fluid: an in-situ approach. *Chem. Geol.* **367**, 70–82 (2014).
59. Chuang, K.-Y. et al. Multidecadal-to-interannual modulations of Late Holocene climate variations reconstructed from oxygen isotope ratios

of a 237-year-long lived fossil coral in Kikai Island, southwestern Japan. *Quat. Sci. Rev.* **322**, 108392 (2023).
60. Sully, S. et al. A global analysis of coral bleaching over the past two decades. *Nat. Commun.* **10**, 1264 (2019).
61. Williams, S. et al. Effects of light and temperature on Mg uptake, growth, and calcification in the proxy climate archive *Clathromorphum compactum*. *Biogeosciences* **15**, 5745–5759 (2018).
62. Lewis, B. & Diaz-Pulido, G. Suitability of three fluorochrome markers for obtaining in situ growth rates of coralline algae. *J. Exp. Mar. Biol. Ecol.* **490**, 64–73 (2017).
63. Schneider, C. A., Rasband, W. S. & Eliceiri, K. W. NIH Image to ImageJ: 25 years of image analysis. *Nat. Methods* **9**, 671–675 (2012).
64. Li, L. et al. Newly described rhodolith bed complex associated with shallow coral reefs of Palmyra Atoll, Northern Line Islands. *Aquat. Conserv. Mar. Freshw. Ecosyst.* **35**, e70024 (2025).
65. Twist, B. A. et al. The need to employ reliable and reproducible species identifications in coralline algal research. *Mar. Ecol. Prog. Ser.* **654**, 225–231 (2020).
66. Richards, J. L. et al. New insights into the genus *Lithophyllum* Lithophylloideae, Corallinaceae, Corallinales from deepwater rhodolith beds offshore the NW Gulf of Mexico. *Phytotaxa* **190**, 1–162 (2014).
67. Giorgi, A. et al. DNA sequencing reveals higher taxonomic diversity of coralline algae (Corallinales and Hapalidiales, Rhodophyta) in the tropical western North Atlantic that complicates ecological studies. *Botanica Marina* **67**, 561–586 (2024).
68. Dewanckele, J., Boone, M. A., Coppens, F., Van Loo, D. & Merkle, A. P. Innovations in laboratory-based dynamic micro-CT to accelerate in situ research. *J. Microsc.* **277**, 197–209 (2020).
69. DeCarlo, T. M. Deriving coral skeletal density from computed tomography (CT): effects of scan and reconstruction settings. *Matters Select* **3**, e201706000005 (2017).
70. Savitzky, A. & Golay, M. J. E. Smoothing and differentiation of data by simplified least squares procedures. *Anal. Chem.* **36**, 1627–1639 (1964).
71. Virtanen, P. et al. SciPy 1.0: fundamental algorithms for scientific computing in Python. *Nat. Methods* **17**, 261–272 (2020).
72. Longerich, H. P., Jackson, S. E. & Günther, D. Laser ablation inductively coupled plasma mass spectrometric transient signal data acquisition and analyte concentration calculation. *J. Anal. At. Spectrom.* **11**, 899–904 (1996).
73. Jochum, K. P. et al. Determination of reference values for NIST SRM 610–617 glasses following ISO guidelines. *Geostand. Geoanal. Res.* **35**, 397–429 (2011).
74. Schöne, B. R. et al. Importance of weighting high-resolution proxy data from bivalve shells to avoid bias caused by sample spot geometry and variability in seasonal growth rate. *Front. Earth Sci.* **10**, 889115 (2022).
75. McCoy, S. J. et al. Calcification in the coralline red algae: a synthesis. *Phycologia* **62**, 648–666 (2023).
76. Meert, W. et al. DTAIDistance, version 2. *Zenodo* https://doi.org/10.5281/zenodo.3981067 (2020).
77. Benjamini, Y. & Hochberg, Y. Controlling the false discovery rate: a practical and powerful approach to multiple testing. *J. R. Stat. Soc. B* **57**, 289–300 (1995).

Acknowledgements

We are grateful to Matthew Tietbohl, Corinne D'Anna, and Huajing Yan for their help with fieldwork. We thank Ute Schmidt for providing the globe in Fig. 1b. We thank Lukas Fröhlich and Julian Schröder for assistance with LA-ICP-MS data reduction. We thank Vincent Saderne for his support of the initial conception of the project. We thank Ronell Sicat and the KAUST Visualization Core Lab for their assistance with Avizo™ image processing. We thank Paula Del Río Gómez and the University of Barcelona CORELAB for their assistance with microCT scanning. We thank Jan Leitner and Michael Maus for their help with sample preparation, and Ulrike Weis, Brigitte Stoll, and Moritz Elsässer for their help with LA-ICP-MS data collection. We thank Janne Repschläger and Anthea Arns for their perspective and valuable input. We thank Aurora Giorgi for her assistance in taxonomic identification. Rhodolith samples were collected in 2024 in accordance with the regulations applicable at the time of collection.

Author contributions

L.Y.L. conceptualized the study. The methodology was developed by L.Y.L. and J.P.B.T. L.Y.L. carried out and visualized all analyses. Funding was acquired by L.Y.L., B.R.S., R.S., H.V., M.D.F., and M.D.J.. W.A.R. provided the in-situ temperature logger data. L.Y.L wrote the original draft, and all authors—L.Y.L., J.P.B.T., S.H., J.H., W.A.R., M.D.F., M.D.J., H.V., R.S., and B.R.S.—contributed to the review and editing of the manuscript.

Funding

This research was supported by the Max Planck Graduate Center with the Johannes Gutenberg-Universität Mainz (MPGC) under the joint supervision of B.R.S., R.S., J.H., and S.H. Fieldwork and SEM imaging were supported by M.D.J.'s KAUST baseline funding. Collection of in-situ temperature data was supported by M.D.F.'s KAUST baseline funding. MicroCT scanning was supported by Francesc Maynou (Institut de Ciències del Mar - CSIC). Open Access funding enabled and organized by Projekt DEAL.

Competing interests

The authors declare no competing interests.

Additional information

Supplementary information The online version contains supplementary material available at https://doi.org/10.1038/s43247-026-03603-y.

Correspondence and requests for materials should be addressed to Lena Y. Li.

Peer review information *Communications Earth and Environment* thanks the anonymous reviewers for their contribution to the peer review of this work. Primary Handling Editor: Alireza Bahadori. A peer review file is available.